The Astrophysical Journal, 889:159 (10pp), 2020 February 1 https://doi.org/10.3847/1538-4357/ab66ae

X-Ray Ionization of Planet-opened Gaps in Protostellar Disks

S. Y. Kim[1,2,3] and N. J. Turner[4]
[1] Division of Physics, Mathematics & Astronomy, California Institute of Technology, Pasadena, CA 91125, USA
[2] Department of Astronomy, Ohio State University, 4055 McPherson Laboratory, 140 West 18th Avenue, Columbus, OH 43210, USA
[3] Department of Physics, University of Surrey, Guildford, Surrey GU2 7XH, UK
[4] Jet Propulsion Laboratory, California Institute of Technology, Pasadena, CA 91109, USA; neal.turner@jpl.nasa.gov
Received 2018 April 11; revised 2019 December 28; accepted 2019 December 30; published 2020 February 4

Abstract

Young planets with masses approaching Jupiter's have tides strong enough to clear gaps around their orbits in the protostellar disk. Gas flow through the gaps regulates the planets' further growth and governs the disk's evolution. Magnetic forces may drive that flow if the gas is sufficiently ionized to couple to the fields. We compute the ionizing effects of the X-rays from the central young star, using Monte Carlo radiative transfer calculations to find the spectrum of Compton-scattered photons reaching the planet's vicinity. The scattered X-rays ionize the gas at rates similar to or greater than the interstellar cosmic-ray rate near planets with the masses of Saturn and of Jupiter, located at 5 au and at 10 au, in disks with the interstellar mass fraction of sub-micron dust and with the dust depleted by a factor 100. Solving a gas–grain recombination reaction network yields charged particle populations whose ability to carry currents is sufficient to partly couple the magnetic fields to the gas around the planet. Most cases can undergo Hall-shear instability, and some can launch magnetocentrifugal winds. However, the material on the planet's orbit has diffusivities so large in all the cases we examine that magnetorotational turbulence is prevented and the non-ideal terms govern the magnetic field's evolution. Thus the flow of gas in the gaps opened by young giant planets depends crucially on the finite conductivity.

Unified Astronomy Thesaurus concepts: Protoplanetary disks (1300); Radiative transfer (1335); Magnetic fields (994); X-ray stars (1823)

1. Introduction

A protoplanet that grows beyond the mass of Saturn has gravity strong enough for its tides to clear an annular gap of low surface density around its orbit in the protostellar disk, as reviewed by Baruteau et al. (2014). The planet can continue to grow only if material from the gap walls is able to reach its Hill sphere. Furthermore, the planet's subsequent orbital evolution is governed by the distribution of gas across the gap, especially the amount of material located near orbital resonances. The orbit's evolution also depends on the rate at which disk material crosses the gap. In this contribution we investigate whether magnetic forces can act on the gap. We explore whether the gas in the gap is ionized well enough to couple to magnetic fields, so that the fields can displace the material near the planet.

Young stars emit ionizing X-rays with temperatures of thousands of electron volts (Feigelson & Montmerle 1999), able to penetrate the circumstellar gas and dust to columns of the order of $10\,\mathrm{g\,cm^{-2}}$ (Glassgold et al. 1997; Ercolano & Glassgold 2013). By comparison, the minimum-mass solar nebula has a surface density at 5 au of about $\Sigma = 150\,\mathrm{g\,cm^{-2}}$ (Weidenschilling 1977; Hayashi 1981). Few stellar X-ray photons thus reach the midplane before planets have grown. However, once a gap opens in the disk, the X-ray flux at the midplane can increase. The gas making up the gap's inner rim will forward-scatter some of the photons arriving from the star, deflecting a fraction down to the planet's vicinity. The gap's outer rim, exposed directly to the optical light from the central star, heats and expands vertically (Turner et al. 2012), intercepting extra X-ray photons, some of which will be scattered backward and down into the gap. A planet opening a gap thus receives more X-rays than a non-gap-opening planet at the same location.

Here we examine whether a gap can increase the X-ray flux enough to contribute significantly to the ionization of gas near the planet. We compute the X-ray intensity in the planet's vicinity using a Monte Carlo radiative transfer approach, estimate the resulting ionization state by integrating a simple ionization–recombination reaction network to equilibrium, and compute the plasma's magnetic diffusivity. We compare against the threshold diffusivities required for the operation of three mechanisms proposed to drive the accretion flow: magnetorotational turbulence, Hall-shear instability (HSI), and magnetocentrifugal winds. We extend work by Keith & Wardle (2015) in carrying out X-ray transfer calculations rather than using results from a gapless disk, while making relatively simple assumptions about the gap structure and the strength and geometry of the magnetic fields.

The paper is laid out as follows. The model star and disk are described in Section 2, the X-ray transfer methods in Section 3. The ionization–recombination chemistry and how we translate the charged species' abundances into diffusivities and magnetic stresses are set out in Section 4. The resulting X-ray spectra, ionization levels, and magnetic coupling are shown in Section 5. Discussion and conclusions follow in Section 6.

2. Star and Disk

Each model consists of a star, disk, and planet. The young star is of solar mass and twice solar radius, and emits a blackbody spectrum with effective temperature 4500 K. The resulting luminosity of $L_* = 1.5$ times solar is in the range indicated by stellar evolution modeling at ages 1–2 Myr (D'Antona & Mazzitelli 1994; Siess et al. 2000). The star is surrounded by an axisymmetric disk laid down on a radiative transfer grid logarithmically spaced in radius with 120 cells from $10^{-1.4}$ to $10^{1.6}$ au (approximately 0.04–40 au). The

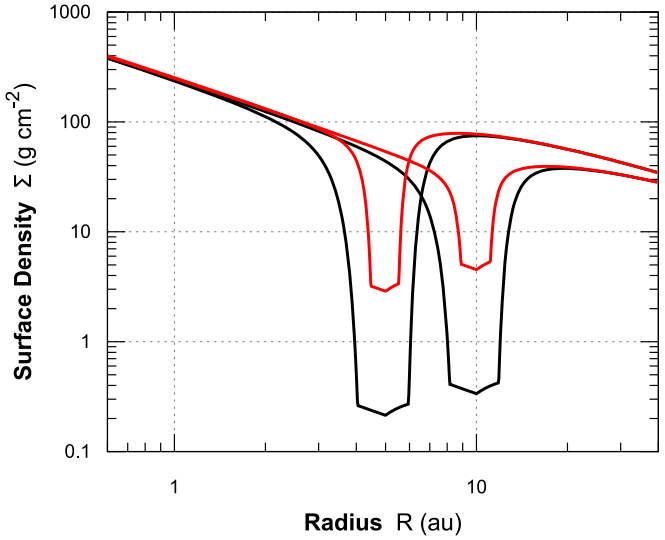

Figure 1. Surface density profiles in the four model protostellar disks, each with a planet the mass of Saturn (red) or Jupiter (black) embedded at 5 or 10 au.

vertical structure is resolved by dividing each annulus into 60 cells spaced uniformly from the midplane up to six initial pressure scale heights.

We adopt disk surface density profiles from a one-dimensional analytic model constructed by Lubow & D'Angelo (2006), in which the planet's gap-opening tidal torques balance the disk's gap-closing viscous stresses (Lin & Papaloizou 1986). The planet follows a fixed circular orbit. The accretion stresses within the disk are modeled using the Shakura–Sunyaev viscous prescription with $\alpha = 0.005$, and the flow is steady-state.

Before any planet is added, the disk's surface density varies inversely with radius, and is 280 g cm^{-2} at 1 au. The planet partly dams the disk's inflow and accretes most of the material reaching its orbit. The ratio of the planet's accretion rate to the flow rate at the same place in the planet-free disk is $E = 6$. This is lower than the $E = 8$ fiducial case of Lubow & D'Angelo (2006) because our model disks have smaller aspect ratios $H/r = 0.034$–0.040 near the planet. Other parameters take the fiducial values from Lubow & D'Angelo (2006).

The analytic model breaks down close to the planet, where horseshoe orbits are important, leading to underestimated densities. In the gap we therefore set densities using the fit to hydrodynamical results by Fung et al. (2014, their Equation (12)). The surface densities in our gaps thus depend on three quantities: α, the planet-to-star mass ratio, and the disk aspect ratio. The gap depths we use are similar to those obtained including the planet's orbital migration (Dürmann & Kley 2015) and in three-dimensional calculations (Fung & Chiang 2016). However, we note that our disk aspect ratio of 0.034 at 5 au lies outside the range 0.04–0.1 covered by these three hydrodynamical works.

We place the planet at either $r_p = 5$ or 10 au, approximating the orbits of Jupiter and Saturn, respectively. To test how magnetic forces can be expected to vary as the planet grows, at each location we consider bodies of both Saturn and Jupiter masses, using planet-to-star mass ratios $q = 3 \times 10^{-4}$ and 10^{-3}, respectively. For the initial midplane temperature profile we adopt $T(r) = 124(L_*/L_\odot)^{1/4}(r/\mathrm{au})^{-1/2}$ K, based on similar radiative transfer calculations without a gap (Turner et al. 2012). This is cooler than the minimum-mass solar nebula because it includes the effects of the disk's large optical depth. The resulting surface density profiles are shown in Figure 1. The gap in all cases has a high enough surface density, thanks to the floor from Fung et al. (2014), that the radial flow speed $v_r = \dot{M}/(2\pi r\Sigma)$ needed to supply the accretion rate is subsonic.

The mass of disk material on the grid ranges from 0.017 $M_\odot$ with a Jupiter at 10 au, to 0.027 $M_\odot$ with a Saturn at 5 au. These are comparable to or a little greater than the minimum-mass solar nebula. We verified that the model disks are not susceptible to fragmentation under their own self-gravity, having the Toomre Q parameter $c_s\Omega/(\pi G\Sigma)$ greater than unity everywhere. Here c_s is the sound speed, Ω the orbital frequency, G the gravitational constant, and Σ the surface mass density. The mass accretion rate in all models is within 1% of $3.3 \times 10^{-8}\,M_\odot\,\mathrm{yr}^{-1}$ outside the planet's orbit, and $5 \times 10^{-9}\,M_\odot\,\mathrm{yr}^{-1}$ inside.

The gap modifies the disk's temperature profile from our initial guess. Evacuating the gap allows the visible light from the central star to directly strike the top of the gap's outer wall. The starlight heats the wall, increasing its internal gas pressure, so in hydrostatic equilibrium the wall becomes taller and intercepts yet more starlight. The tall wall is likely to intercept more of the stellar X-rays too. We therefore include these effects, using an iterative procedure similar to Turner et al. (2012). Given a density distribution, we obtain new temperatures under radiative balance with the optical starlight using Monte Carlo transfer with the relaxation method of Bjorkman & Wood (2001). We then displace gas up or down to restore vertical hydrostatic balance, holding fixed the variation of temperature with column. The new density distribution serves as the input for the next iteration. We quit after five iterations when the structure no longer changes significantly.

The disk's opacity to the optical starlight and reprocessed infrared radiation comes from dust grains. We take dust opacities from Preibisch et al. (1993), where the particle size distribution

$$n(a) \propto a^{-p}, \qquad a_{\min} < a < a_{\max}, \tag{1}$$

with $p = 3.5$. At temperatures below 125 K, the grains are composed of a silicate core and an icy mantle whose radius is 14% of the core's. The mantle is polluted with tiny amorphous carbon grains ($a_{\min} = 0.007\,\mu$m, $a_{\max} = 0.03\,\mu$m). Above 125 K, the icy mantle sublimates, baring a silicate grain ($a_{\min} = 0.04\,\mu$m, $a_{\max} = 1\,\mu$m) and releasing the amorphous carbon grains; the silicates sublimate at 1500 K, the carbon grains at 2000 K. The grains are well mixed in the gas, and we assume the scattering that makes up part of the starlight opacity is isotropic. To model small grains' incorporation into larger bodies, which is likely to have occurred by the time planets grow to Saturn or Jupiter mass, we also compute models with the dust opacities multiplied by a factor $\epsilon = 10^{-2}$. Considering two values each for the planet location, the planet mass, and the dust abundance, we compute the eight model disks listed in Table 1. Each model is given a name whose first digits are the planet location in au, followed by a letter indicating that the planet has Saturn (S) or Jupiter (J) mass, and a final digit that is the logarithm of the factor by which the dust abundance is reduced.

Table 1
X-Ray Ionization Rates at the Planet in the Eight Models

Model	Radius r_p (au)	Mass Ratio q	Dust Depletion ϵ	Column (g cm^{-2})	Ionization Rate $\zeta(r_p, z = 0)$ (s^{-1})	Ratio to IG99 Fit
10S0	10	3×10^{-4}	1	2.26	2.8×10^{-17}	0.71
10S2	10	3×10^{-4}	0.01	2.26	6.8×10^{-17}	1.7
10J0	10	10^{-3}	1	0.168	3.2×10^{-16}	6.3
10J2	10	10^{-3}	0.01	0.168	3.9×10^{-16}	7.7
5S0	5	3×10^{-4}	1	1.45	1.8×10^{-16}	1.0
5S2	5	3×10^{-4}	0.01	1.45	4.2×10^{-16}	2.4
5J0	5	10^{-3}	1	0.107	2.1×10^{-15}	10
5J2	5	10^{-3}	0.01	0.107	2.3×10^{-15}	11

3. X-Ray Ionization

We compute X-ray ionization rates in each model disk by sampling the X-ray mean intensity using Monte Carlo techniques, and converting the absorbed X-ray energies into ionization rates. In most respects we follow Igea & Glassgold (1999, hereafter IG99). In the sections below we sketch the IG99 approach and note our points of departure.

3.1. X-Ray Source

Magnetic reconnection heats plasma in the young star's corona to temperatures exceeding $kT_X = 1$ keV. The plasma emits X-rays by thermal bremsstrahlung, whose spectral luminosity at energy E we approximate by

$$L(E) = \frac{L_X}{kT_X} \exp\left(-\frac{E}{kT_X}\right), \quad (2)$$

where L_X is the total X-ray luminosity and T_X is the source temperature. A less approximate treatment would involve quantum electrodynamic corrections. An electron-velocity-distribution-averaged Gaunt factor that has been set to unity in deriving Equation (2) would then decline by a factor four across the energy range from 1 to 30 keV, tilting the spectrum toward low energies (Karzas & Latter 1961). This would yield higher ionization rates in the disk's surface layers, and lower rates in the interior. However, we follow IG99 in using Equation (2).

Also like IG99, we locate the X-ray source in a helmet streamer taking the shape of a ring centered on the rotation axis, whose radius and height above the disk midplane are each ten times the stellar radius. We adopt a source temperature $T_X = 5$ keV and an X-ray luminosity $L_X = 2 \times 10^{30}$ erg s^{-1}, the median for solar-mass stars in the Orion Nebula Cluster (Garmire et al. 2000). We consider X-rays below 1 keV to be attenuated in the star's magnetosphere and inner wind. We thus compute the transfer of X-rays with energies from 1 keV up to 30 keV.

3.2. X-Ray Opacities

IG99 used a simple power-law energy dependence for the X-ray absorption cross section, and carried out their Monte Carlo calculations assuming that all heavy elements were segregated from the gas. We adopt a more detailed fit by Bethell & Bergin (2011a), who for solar elemental abundances find a cross section of the form

$$\sigma_{tot} = \sigma_{gas} + \epsilon f_b(E)\sigma_{dust}, \quad (3)$$

where ϵ and f_b are the dust settling and grain growth parameters, respectively, and the cross sections of the gas and dust are each given by

$$\sigma(E) = 10^{-24}\ \mathrm{cm}^2 \times (c_0 + c_1 E + c_2 E^2) E^{-3}, \quad (4)$$

with different fitting coefficients c_i for dust and gas. The coefficients are piecewise linear functions of energy, to reproduce discontinuous increases in the absorption opacity due to K-shell photoelectric absorption by various metals. Bethell & Bergin (2011a) provide fits up to 10 keV; we extrapolate to higher energies. Consistent with the optical and infrared transfer, we consider both $\epsilon = 1$ and $\epsilon = 0.01$ to allow for the depletion of small grains. The dust growth parameter f_b is unity for all our calculations. Like IG99 we take the scattering cross section from the Klein–Nishina formula. Cross sections are converted to opacities using a mean gas molecular weight of 2.3, corresponding to solar composition with the hydrogen in molecular form. The energy dependence of the opacities is shown in Figure 2. The scattering cross section is almost constant across the energy range shown, falling off very slightly toward the top end. The absorption falls off much more steeply with photon energy. Thus the albedo $\omega = \sigma/(\kappa + \sigma)$, where κ is the absorption and σ is the scattering opacity, increases dramatically with energy. The highest-energy photons are more likely to be scattered than absorbed. This contributes to the harder X-rays penetrating deeper into the disk.

3.3. X-Ray Transfer and Ionization Rate

We sample the X-rays' mean intensities on the radiative transfer grid using a Monte Carlo approach. We follow each packet of X-ray photons from its emission at the stellar source into the disk and through as many scatterings as needed until the packet either escapes the domain or is absorbed. We assume that all absorbed X-ray energy is converted into ionization. A scattered X-ray packet's new direction is chosen randomly from the Klein–Nishina phase function, and its energy is reduced by Compton losses.

X-ray sources with different energies produce mutually independent intensities in the disk. We therefore perform the Monte Carlo procedure separately for each monochromatic source energy. To construct the desired source spectrum we linearly combine the intensities produced by the monochromatic sources. The resulting mean X-ray intensity is converted to an ionization rate by dividing by the average energy required

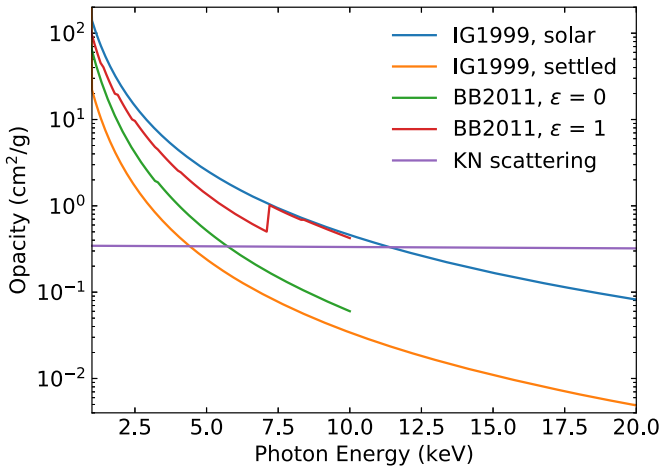

Figure 2. X-ray scattering and absorption opacities. The nearly horizontal line denotes the scattering opacity derived from the Klein–Nishina formula. The absorption opacities, from top to bottom, are (1) IG99's power-law fit assuming solar abundances, (2) Bethell & Bergin (2011a)'s more detailed fit with dust undepleted and (3) fully depleted, and (4) IG99's power-law fit for solar abundance but with heavy elements depleted onto grains that have been removed by settling and growth. We use the opacities of Bethell & Bergin.

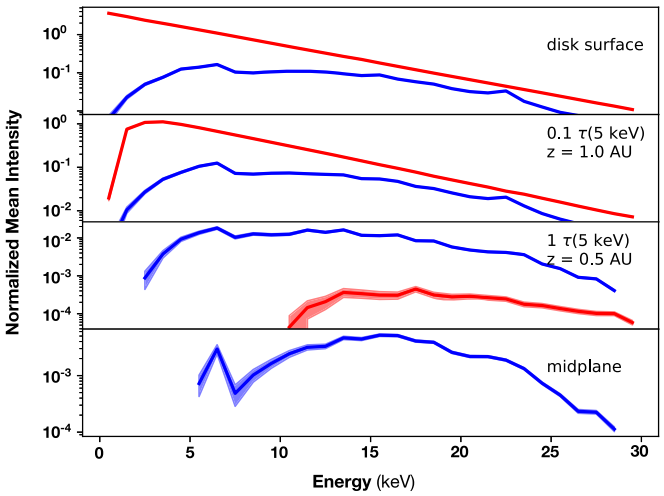

Figure 3. X-ray spectra in model 10S0 at four locations above the planet. The top panel is at the disk surface, the next two are 1.0 and 0.5 au above the planet, and the bottom panel is at the midplane, on the planet's orbit. Each is labeled with the vertical optical depth at 5 keV. Red curves show the photons received directly from the source, and blue curves the scattered photons. Each curve is surrounded by lighter shading marking the $1/\sqrt{N}$ uncertainty in the Monte Carlo results. All are normalized to the mean intensity (erg cm^{-2} sr^{-1} s^{-1} keV^{-1}) at the disk surface at 5 keV. Direct photons are thoroughly absorbed for vertical optical depths unity and greater. Only X-rays with energies over 5 keV reach the midplane in significant numbers, and all these have been scattered.

to produce an ion pair, for which we follow IG99 and adopt the value $\Delta E = 37$ eV.

We differ from IG99 in how we compute the mean intensity. They average over the projected area met by each packet at each radiative transfer grid cell. We instead follow Lucy (1999) in integrating the photon packet's contribution all along its path. This yields lower Monte Carlo noise for a given number of packets, particularly in the optically thin disk atmosphere.

As shown in the top panel of Figure 3, the source spectrum is adequately represented with 30 energy bins. Thus, for each of 30 monochromatic X-ray source energies, uniformly spaced from 1 to 30 keV, we send 10^6 photon packets into our model disks, then construct a weighted sum of the monochromatic results to determine ionization rates for a source with a thermal bremsstrahlung spectrum at a temperature of 5 keV.

4. Magnetic Coupling

4.1. Ionization State

We compute the ionization state by balancing the X-ray ionization with a recombination reaction network including grain surface reactions and simplified gas-phase chemistry (model 4 of Ilgner & Nelson 2006). This yields the equilibrium abundances of seven charged species: electrons, a representative molecular ion (HCO^+), a representative metal ion (Mg^+), and grains charged by one and two electrons either side of neutral.

The magnesium has abundance 3.39×10^{-7} atoms per hydrogen nucleus, 1% of the solar value, since most of the magnesium is locked up in minerals and only a minority can react on the grain surfaces or in the gas phase. The fraction of magnesium in available form has little impact on the ionization balance, since temperatures are low enough that most magnesium atoms stay adsorbed on the grains.

The grains' abundances in the reaction network match those in the corresponding starlight and X-ray radiative transfer calculations, in the following approximate sense. The reaction network treats grains of a single radius, which we set to 0.1 μm. When combined with a material density of 2 g cm^{-3}, this nearly matches the geometric cross section per unit mass in the optical opacity model. Extending the grain population from a single size to a power-law size distribution yields recombination rates that depend a little less steeply than linearly on the total cross section (Bai & Goodman 2009).

4.2. Magnetic Field Strengths

We evaluate three scenarios for whether magnetic torques can drive the accretion flow: (1) magnetorotational turbulence (henceforth MRT), (2) the HSI, and (3) a magnetocentrifugal wind launched from the disk surface. The MRT sustains a tangled field with strong azimuthal and moderate radial components, on a weaker vertical background field. HSI couples the Hall term's rotation of toroidal into radial field, together with the orbital shear's stretching-out of the radial component to generate fresh toroidal field. The resulting fields have a dominant toroidal component. The magnetocentrifugal winds we consider have all three field components comparable near the disk surface.

For each scenario to produce the accretion rates present in the model disk, the field must reach a certain minimum strength, as follows. Taking the equation of motion in cylindrical coordinates (r, ϕ, z), reducing to the case of a near-axisymmetric, near-Keplerian disk with time-steady mean internal flows, and averaging over the disk thickness $2h$, yields

$$\frac{\dot{M}\Omega}{2r} = \frac{2h}{r}\langle -B_r B_\phi \rangle + \frac{\partial}{\partial r}[h\langle -B_r B_\phi \rangle] - (B_z B_\phi)_s, \qquad (5)$$

where angle brackets denote averages through the disk, and the subscript s marks fields measured on the disk's top and bottom surfaces (Wardle 2007). The first two terms on the right come from magnetic stresses in the disk interior, for example due to MRT or HSI, while the final term is the wind's back-reaction on the disk via magnetic torques. As is common, we assume

that the mean stress varies only over length scales at least comparable to the radius, so that the second term is comparable to or smaller than the first, and can be neglected.

In the MRT scenario, angular momentum conservation thus links the mass flow rate $\dot{M}$ carried by the disk to the magnetic accretion stress by

$$\langle -B_r B_\phi \rangle = \frac{\dot{M}\Omega}{4h}. \quad (6)$$

The stress from the field's radial and azimuthal components is about one-quarter the squared magnitude of the magnetic field, which in turn is about 20 times the mean squared vertical field, based on direct numerical calculations (Hawley et al. 1995; Sano et al. 2004). We can thus solve Equation (6) for the rms vertical field.

Equation (6) also gives the stress in the HSI scenario. To find the mean vertical field strength, we observe that the toroidal component is about 50 and 200 times the radial and vertical components in Lesur et al. (2014, run 1-OHA-5).

In the wind scenario, Equation (5) becomes

$$(-B_z B_\phi)_s = \frac{\dot{M}\Omega}{2r}, \quad (7)$$

where the subscript s indicates values measured at the disk surface. We estimate the vertical field using the fact that magnetocentrifugal wind solutions typically have the three field components roughly equal at the disk surface. The surface connects the interior, with its vertical magnetic field, to the wind, where the field is angled away from the rotation axis.

4.3. Coupling Criteria

With the field strength in hand from Equation (6) or (7), and the charged species' abundances from Section 4.1, we can find the magnetic diffusivities and determine whether the field in fact couples to the gas well enough to drive the accretion flow.

We compute the diffusivities η_O, η_H, and η_A that are the coefficients of the ohmic, Hall and ambipolar terms in the induction equation, including the contributions from all charged species, following Equations (21)–(31) of Wardle (2007). The diffusivities depend on the field strength, which governs whether each charged species mostly gyrates around the field lines under the Lorentz force or mostly random-walks by colliding with neutrals.

Each of the three magnetic scenarios works only when the diffusivities and field strengths meet a set of requirements. For MRT, disturbances with the linear magnetorotational instability's fastest-growing wavelength must diffuse away more slowly than they grow. The wavelength v_{Az}/Ω depends on the Alfvén speed v_{Az} along the vertical magnetic field, the growth rate is close to Ω, and the relevant diffusivity is the sum of the ohmic and ambipolar values, called the Pedersen diffusivity $\eta_P = \eta_O + \eta_A$. Thus MRT requires

$$\eta_P < v_{Az}^2/\Omega \quad (8)$$

(Sano & Inutsuka 2001; Turner et al. 2007; Keith & Wardle 2015). In addition the wavelength must fit within the disk thickness, corresponding to a vertical magnetic field with pressure less than that of the gas by a factor

$$\beta_z > 8\pi^2 \quad (9)$$

(Okuzumi & Hirose 2011). At the same time, the Hall term must be small enough to not much modify the character of the turbulence. Lesur et al. (2014) find that the Hall term dominates if the Hall length exceeds 20% of the gas scale height. The Hall length is $|\eta_H|/v_A$, thus standard MRT requires approximately

$$|\eta_H| < \beta_z^{1/2} v_{Az}^2/\Omega. \quad (10)$$

For the HSI in contrast, a strong Hall term is required: the Hall diffusivity must exceed the right-hand side of relation (10). Furthermore a large Hall term appears able to drive instability even in the face of significant ohmic and ambipolar diffusion (Lesur et al. 2014). We therefore place no upper limit on the Pedersen diffusivity under which the Hall-shear process can operate. If the fastest-growing wavelength were the determining factor, too strong a magnetic field would again be disqualifying, and relation (9) would also be a requirement for HSI (Keith & Wardle 2015). However, we note that the spectrum of unstable linear modes can extend to wavelengths shorter than the ideal-MHD cutoff if the Hall term is strong (Sano & Stone 2002), and that the HSI operates with a midplane plasma beta near unity in run 1-OHA-5 of Lesur et al. (2014). For these reasons we do not limit the field strengths at which HSI is allowed.

Finally, to launch a magnetocentrifugal wind, the disk must be able to sustain vertical gradients in the field's horizontal components. That is, the fields may not diffuse through the disk thickness in less than one orbit. This boils down to

$$\eta_{max} < c_s^2/\Omega, \quad (11)$$

where η_{max} is whichever is larger, η_P or η_H (Keith & Wardle 2015).

To summarize, each magnetic scenario and mass flow rate jointly imply a field strength, which together with the charged species' populations yields the diffusivities. The MRT scenario is viable if the field and diffusivities satisfy relations (8)–(10). The Hall-shear scenario is viable if the negation of relation (10) holds. The magnetized wind is viable given relation (11). To express these requirements compactly below, we define $\eta_{v_{Az}} \equiv v_{Az}^2/\Omega$ and $\eta_{c_s} \equiv c_s^2/\Omega$.

5. Results

5.1. X-Ray Spectra

In all cases, the X-rays reach the midplane with a much lower intensity than in the disk atmosphere, and a spectrum favoring higher energies. In Figure 3 are the spectra observed at four heights above the planet in model 10S0. The lower-energy direct X-rays are absorbed high in the atmosphere, while the intensity of higher-energy photons declines with depth, as Compton downscattering converts them to lower energies where they are more easily absorbed. Few or no photons reach the planet with energies below 10 keV, while the intensity at energies above 10 keV is around 0.1% of that expected in the absence of the intervening disk material. Almost all photons reaching the midplane were emitted from the source with energies above 18 keV. The 8 keV dip in the spectrum at intermediate heights comes from the iron absorption edge near 7 keV, visible in Figure 2.

The cleaner gaps opened by the Jupiters let more photons with energies below 10 keV reach the planet's vicinity (Figure 4). Still most of the ionization comes from photons emitted with energies above 10 keV, many of which scatter

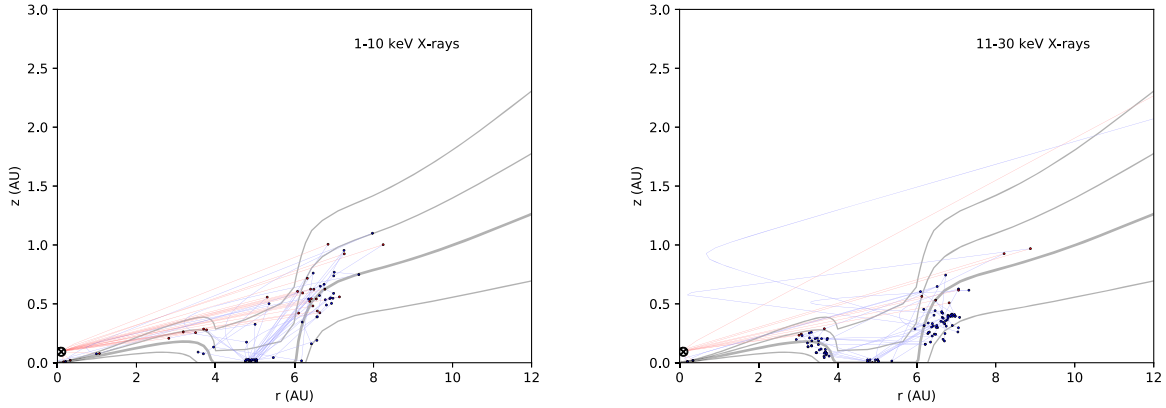

Figure 4. Paths in the (r, z) plane of photon packets chosen randomly from among those reaching the planet's vicinity in model 5J0, which has a Jupiter-mass planet at 5 au in a dusty disk. The X-ray source is marked by the cross in a circle near (0.1, 0.1) au. Each path is red before the first scattering, and blue thereafter. Filled circles mark scattering points. The thick gray line shows the surface of unit vertical optical depth to 5 keV photons, while thin gray lines denote optical depths spaced by factors of 10. The first panel shows photons with energies up to 10 keV, for which the single-scattering albedo is below 50%. Most photons reaching the planet are scattered just once off the gap rim. The second panel is for higher-energy, higher-albedo photons, which often scatter repeatedly off the gap walls. Some scatter first in the disk surface layers interior to the gap, and a few pass near the rotation axis as they cross from one side of the disk to the other. The number of packets in each panel is in proportion to the energy band's contribution to ionization near the planet.

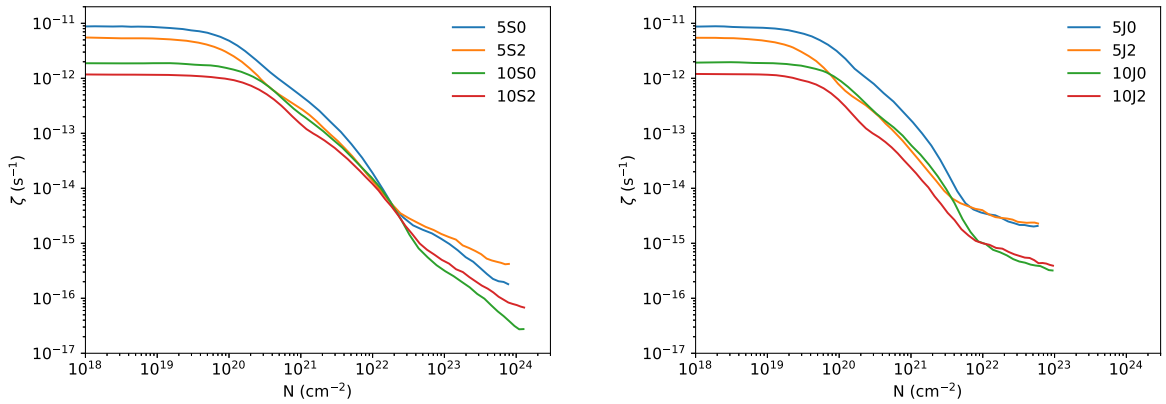

Figure 5. Ionization rates vs. vertical column of hydrogen nuclei, above planets with the mass of Saturn (left) and Jupiter (right). The X-rays ionize faster than $10^{-16}\,s^{-1}$ in all models except those with the Saturn at 10 au.

more than once because their single-scattering albedos exceed one-half.

5.2. Ionization Rates

The ionization rates for all models are plotted in Figure 5 versus the column perpendicular to the midplane. In all cases the rates are column-independent in the optically thin upper layers, where they are fixed by the flux of the numerous low-energy X-rays. At greater columns, the disk is optically thick to the softer X-rays, precipitating a sharp decline in the ionization rate. A scattering shoulder appears at columns greater than $N_H = 10^{22}\,cm^{-2}$, or vertical 5 keV optical depths greater than 0.05, where the contribution from scattered harder X-rays extends ionization into the disk interior. The ionization rate asymptotes at the highest columns in the Jupiter cases, because the total X-ray optical depth is low, so all points near the midplane see the remaining scattered X-rays.

At greater distances from the star, X-rays are less important because of the inverse-square falloff in their flux. It is thus worth considering whether the X-rays are competitive with the interstellar cosmic rays. These are attenuated by the protostar's wind (Cleeves et al. 2013), although the latter was likely funneled by the disk and its wind into a bipolar configuration. While the disk at 10 au could receive some cosmic rays focused by the disk wind or entering near the equatorial plane, molecular abundances observed at tens of au in at least one disk are well fit by a model without cosmic rays (Cleeves et al. 2015). Thus the cosmic-ray ionization rate inside 10 au is likely well below the interstellar value of about $10^{-17}\,s^{-1}$. Thermal ionization and radionuclide decay ionization (Umebayashi & Nakano 2009) are orders of magnitude weaker still at 5 and 10 au.

X-ray ionization rates at the planet exceed $10^{-16}\,s^{-1}$ in all the models we consider except those with a Saturn-mass planet at 10 au. Specifically, the X-ray ionization rates listed in the next-to-last column of Table 1 are around 3×10^{-17} and $3 \times 10^{-16}\,s^{-1}$ for a Saturn- and a Jupiter-mass planet, respectively, at 10 au. Moving the planet inward to 5 au increases the ionization rate about one order of magnitude. Reducing the dust abundance increases the X-ray albedo and so the ionization rate near the planet.

The final column in Table 1 shows the ratio of the ionization rate near the planet to that at the same radius and mass column in the fit to the IG99 results (Turner & Sano 2008) that was considered by Keith & Wardle (2015). The ratio exceeds unity for almost all the models. Three factors contribute. First, where IG99 ended their calculations at 20 keV, we include photons emitted with energies up to 30 keV, raising ionization

Table 2
Magnetic Field Strengths (mG) Yielding Disk Models' Mass Flow Rates

Model	$\dot{M}$ ($10^{-8}\,M_\odot\,\mathrm{yr}^{-1}$)	MRT		HSI		MCW	
		B	B_z	B	B_z	B_s	B_z
10S0	0.5	17	3.9	62	0.31	4.5	2.6
	3.3	45	10	160	0.79	11	6.6
10S2	0.5	16	3.6	58	0.28	4.5	2.6
	3.3	41	9.2	150	0.73	11	6.6
10J0	0.5	16	3.7	58	0.29	4.5	2.6
	3.3	42	9.4	150	0.75	11	6.6
10J2	0.5	15	3.4	54	0.27	4.5	2.6
	3.3	40	8.8	140	0.7	11	6.6
5S0	0.5	46	10	160	0.82	11	6.1
	3.3	120	27	420	2.1	27	16
5S2	0.5	42	9.5	150	0.75	11	6.1
	3.3	110	24	390	1.9	27	16
5J0	0.5	44	9.7	150	0.77	11	6.1
	3.3	110	25	400	2	27	16
5J2	0.5	41	9.2	150	0.73	11	6.1
	3.3	110	24	370	1.9	27	16

rates by about 10% at the planet in the case shown in Figure 3. The X-ray source spectrum's steepness means that further increases in the upper energy limit would yield rises in the ionization rate at the level of a few per cent at most. Second, IG99 assumed that dust growth and settling removed all elements heavier than helium, while we include these elements (Figure 2), raising by a factor of a few the fraction of X-rays absorbed per unit column (Ercolano & Glassgold 2013), in particular among those photons that survive to reach the planet. Third, the gap rims scatter photons toward the planet (Figure 4). Only the last of these three factors depends on the planet's mass, so the greater enhancement over IG99 in our models with Jupiters indicates the importance of scattering from the rims.

5.3. Magnetic Coupling

Inserting the ionization rates in the reaction network and evolving to chemical equilibrium yields the ionization states. For the dusty cases with Saturn-mass planets, the most abundant positive and negative species at the planet's location are molecular ions and grains with one extra electron, respectively. In all other cases, the most abundant are molecular ions and free electrons. However, in the hottest case, with the Jupiter in the dust-depleted disk, enough metal atoms are desorbed into the gas that the metal ions are almost as abundant as the molecular ions.

The charged species' movements, and thus the diffusivities, depend on the magnetic field strength as discussed in Section 4.3. In addition, the coupling criteria (8)–(10) are explicit functions of the field's vertical component. Thus in Table 2 we list the total and vertical field strengths just inside and outside the planet's orbit, obtained using Equations (6) and (7) from the corresponding mass flow rates of 5×10^{-9} and $3.3 \times 10^{-8}\,M_\odot\,\mathrm{yr}^{-1}$ respectively. The field strengths are listed to two significant figures.

We combine the charged particle populations with the field strengths in each of the three magnetic scenarios, to obtain the ohmic, Hall, and ambipolar diffusivities. The coupling criteria are then fully specified and we can evaluate whether each scenario is viable, in the sense that its field strength yields diffusivities that permit the scenario to occur. The results for locations just inside and outside the planet's orbit appear in Table 3. Checks mark scenarios that meet the conditions according to the dimensionless numbers in columns 6–9. These in turn come from relations (8) to (11) with magnetic fields from the corresponding scenarios. The dimensionless numbers are rounded to one significant figure.

In all cases, the MRT scenario yields a large ambipolar contribution to the Pedersen diffusivity, which is strong enough to invalidate the assumption that magnetorotational turbulence is present. In some cases, the MRT scenario is also ruled out because it requires fields that are too strong for the magnetorotational wavelength to fit into the disk thickness. In no case is the MRT prevented solely by the Hall diffusivity; thus we do not list the MRT scenario's Hall number in Table 3. In contrast, the HSI scenario implies magnetic fields such that the Hall length is great enough for the HSI to operate in all except the two dust-depleted Jupiter cases, where there is a difficulty outside the planet's orbit. In many of the dust-depleted cases, which tend to be better ionized, the maximum diffusivity is low enough for the gas near the gap's midplane to act as the base for a magnetocentrifugal wind (MCW).

Profiles of the magnetic coupling through the column of material above the planet are shown in Figure 6. The two cases plotted here bracket the range of the full set of models. The first, 10S0, has conditions least favorable for ionization: the planet lies far from the X-ray source, the full dust abundance means both greater X-ray optical depth and rapid recombination on grain surfaces, and the relatively large gas column in the gap likewise makes recombination quick. The other case in Figure 6, model 5J2, is at the opposite extreme in all these respects, and has the highest midplane ionization fraction of all our models.

Because the X-ray intensity rises with height above the planet, while the recombination rate declines as the square of the density, the ionization fraction rises with height. In model 10S0, this means a fairly well-coupled layer at intermediate heights, while still further up, the declining density makes the ambipolar diffusivity dominant. In model 5J2, lower gas densities and higher ionization rates mean the fairly well-coupled layer reaches down to the midplane. These trends in the three non-ideal magnetic diffusivities with mass column are similar to those in modeling of protostellar disks without gaps, for example by Wardle (2007) and Bai (2011, 2014).

The coupling conditions shown in Figure 6 have the following implications for the three magnetic scenarios. From the top left panel, we see that in the 10S0 model under the turbulent scenario, the magnetic field near the midplane is weak enough to be consistent with magnetorotational turbulence (red shading), but the diffusivity is too large for the instability to operate (the blue and green curves are below unity). Conversely in the atmosphere, the Hall diffusivity is low enough for turbulence (blue shading), but the field is too strong to allow it. Ambipolar diffusion is an obstacle to turbulence everywhere (green curve). The situation is still less favorable for magnetorotational turbulence in the 5J2 model (top right panel), because the magnetic field is too strong even at the midplane. The middle row of panels shows that the criterion for HSI is satisfied throughout the 10S0 model, and in three distinct layers in the 5J2 model (blue shading). The panels in the bottom row show that a magnetocentrifugal wind can be launched from a surface layer in the 10S0 case, and from the midplane up to half a scale height or so in the 5J2 case.

Table 3
Magnetic Scenarios' Viability Just inside and outside the Planet's Orbit

Model	$\dot{M}/10^{-8}$ ($M_\odot$ yr^{-1})	MRT	HSI	Wind	MRT η_{vAz}/η_P	MRT β_z	HSI $\beta_z^{1/2}\eta_{vAz}/\lvert\eta_H\rvert$	Wind η_{cs}/η_{max}
10S0	0.5	⋯	✓	⋯	6e−4	8e+2	7e−4	3e−1
	3.3	⋯	✓	⋯	4e−3	1e+2	7e−4	2e−1
10S2	0.5	⋯	✓	✓	4e−2	1e+3	2e−2	5e+1
	3.3	⋯	✓	✓	4e−2	2e+2	2e−2	2e+1
10J0	0.5	⋯	✓	✓	1e−2	8e+1	1e−3	5e+0
	3.3	⋯	✓	⋯	2e−2	1e+1	9e−4	8e−1
10J2	0.5	⋯	✓	✓	3e−2	1e+2	6e−2	2e+1
	3.3	⋯	⋯	✓	3e−2	2e+1	1e+0	3e+0
5S0	0.5	⋯	✓	⋯	2e−3	3e+2	9e−4	4e−1
	3.3	⋯	✓	⋯	1e−2	4e+1	9e−4	3e−1
5S2	0.5	⋯	✓	✓	5e−2	4e+2	2e−2	3e+1
	3.3	⋯	✓	✓	5e−2	5e+1	2e−2	1e+1
5J0	0.5	⋯	✓	✓	2e−2	2e+1	1e−3	4e+0
	3.3	⋯	✓	⋯	2e−2	4e+0	6e−4	6e−1
5J2	0.5	⋯	✓	✓	4e−2	3e+1	8e−2	1e+1
	3.3	⋯	⋯	✓	4e−2	4e+0	1e+0	2e+0

The launching layers' shallowness might suggest that the wind does not reach escape speed before ambipolar diffusion decouples it from the fields, ending magnetic acceleration and collimation. However, ambipolar diffusion can also heat the wind (Safier 1993) enough to increase its ionization beyond that provided by the X-rays. Furthermore, much greater ionization is expected high in the atmosphere, where the stellar far-ultraviolet photons are absorbed (Bethell & Bergin 2011b; Perez-Becker & Chiang 2011). Since we treat neither ambipolar heating nor far-UV photons, our calculations are not valid higher in the outflow. Determining the fate of the wind would furthermore require non-ideal MHD calculations spanning the gap and the nearby disk, where launching conditions may be quite different from the gap.

A note of caution is in order regarding timescales in the 5J2 model, with the Jupiter-mass planet at 5 au in the dust-depleted disk. Gas flows from the gap edge to the planet in about 100 yr, similar to the time for the reaction network to reach equilibrium at the midplane. The ionization state in the gap will therefore be intermediate between our local equilibrium values and conditions upstream in the outer rim. Since the denser rim material has slower ionization and faster recombination, this will mean the gap is more poorly coupled to the magnetic fields than in Table 3 and Figure 6.

6. Discussion and Conclusions

We have carried out transfer calculations for X-rays emitted from the corona of a young star into a surrounding protostellar disk containing an embedded Saturn- or Jupiter-mass planet. The distribution of the material through which the X-rays pass is determined by the planet's tides, which open a gap in the disk, and by the optical starlight, whose heating effects determine the disk thickness under our assumption of vertical hydrostatic equilibrium. Some of the X-rays scattered in the disk atmosphere reach and ionize the gas in the planet's vicinity. The ionization rates are comparable to or greater than those produced in the interstellar medium by cosmic rays. Ionization rates near the Jupiters are up to one order of magnitude greater than at the same distance and column in the standard IG99 fit, owing to the scattering from the gap's rims. Ultraviolet radiation, which we do not treat, could further ionize the planet's vicinity in the Jupiter cases. However, the Saturn cases' greater column density, which far exceeds the absorption depth of ultraviolet photons, means there are few options for raising the ionization rate near the planet above that provided by the X-rays.

The ionization rates depend mostly on the shape of the gap and the column of material within. The magnetic coupling results summarized next depend also on the recombination chemistry and magnetic field strength and orientation, for which the ranges of possibilities are wide. The coupling results should therefore be considered less certain.

We compute the equilibrium ionization state of the material near the planet using a simplified chemical reaction network including representative molecular and metal ions, and recombination on grain surfaces. From the populations of charged species, we compute the ohmic, Hall, and ambipolar diffusivities under three scenarios for the magnetic fields: the accretion flow is driven by either (1) magnetorotational turbulence, (2) HSI, or (3) a magnetocentrifugal wind.

In all cases, the diffusivity is too high for magnetorotational turbulence to transport angular momentum in the gas near the planet. Ambipolar diffusion decouples the magnetic fields from the disk's neutral component over the length and timescales that would be associated with the turbulence. HSI, in contrast, can drive the accretion flow in almost all cases: the field strengths needed for HSI to produce the assumed mass flow rates yield Hall diffusivities great enough for the HSI to operate. This fails only in the models with a Jupiter in a dust-depleted disk. A scenario with a magnetocentrifugal wind also appears viable in the less-diffusive cases we considered, especially if ultraviolet ionization or ambipolar heating sustains coupling at heights above where the X-rays are important. In particular, a wind can begin near the planet in all the dust-depleted scenarios.

Overall, the X-rays leave material near the planet marginally ionized, so that magnetic forces can alter the material's distribution and impact the planet's growth and orbital migration, yet magnetorotational turbulence is unlikely.

While each of our models is static, together they suggest the following evolutionary sequence. A young planetary system develops as the disk's solid material is incorporated into rocks,

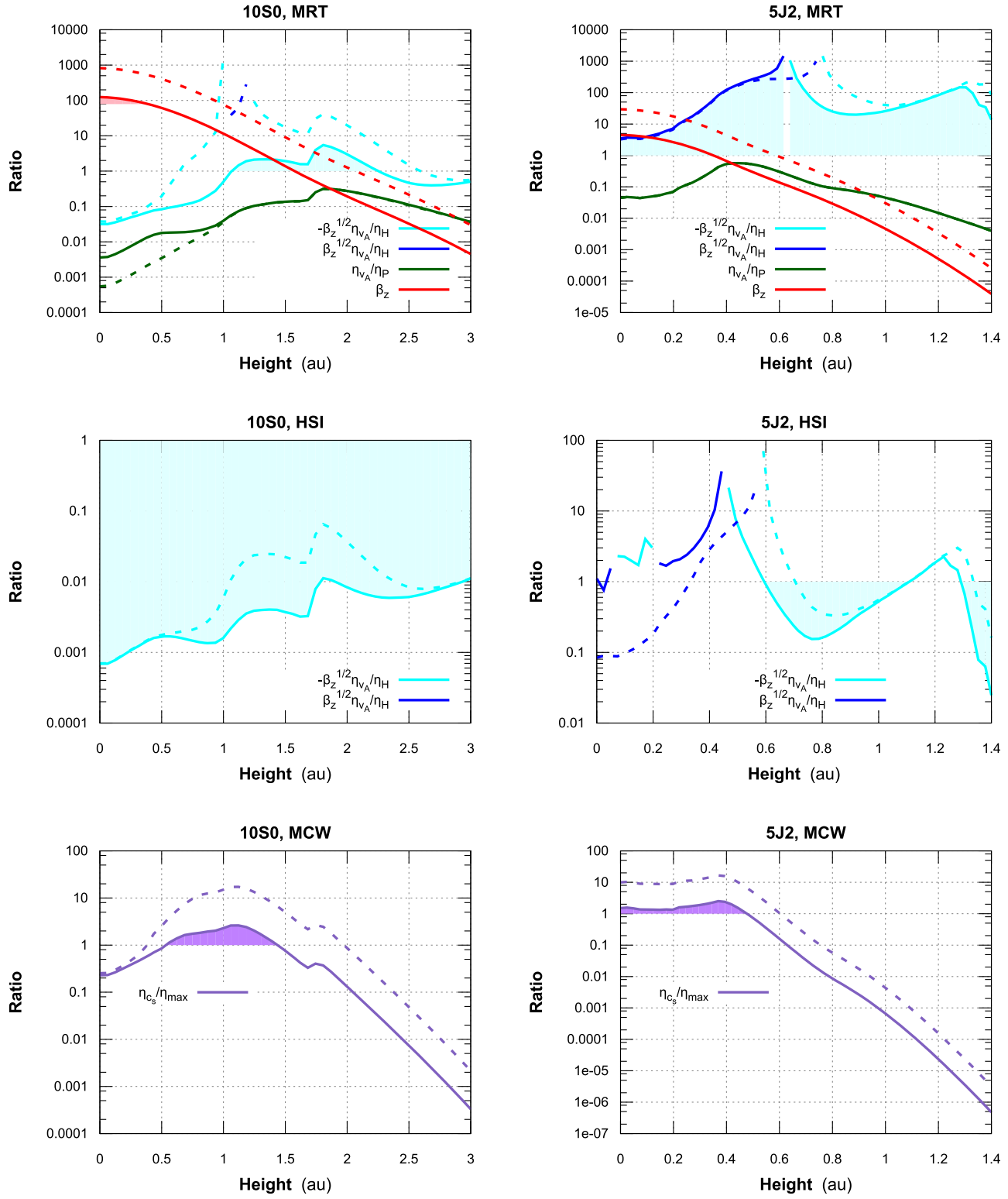

Figure 6. Viability of the magnetorotational turbulence (MRT), Hall-shear instability (HSI), and magnetocentrifugal wind (MCW) scenarios (top to bottom), in the models with a Saturn in a dusty disk (10S0, left column) and a Jupiter in a dust-depleted disk (5J2, right column). Solid curves are for the mass flow rate found just outside the planet's orbit, dashed curves for the lower rate just inside the orbit. Shading marks the portion of each solid curve that meets the constraints of relations (8) (green), (9) (red), (10) (blue), and (11) (purple). Darker sections of the blue curves show where the Hall diffusivity is positive. The MRT scenario jointly meets its three constraints nowhere. The HSI scenario is viable everywhere in the Saturn case, and in three distinct layers in the Jupiter case. MCW yields diffusivities consistent with its own operation in the Saturn case in a layer of the disk atmosphere, and in the Jupiter case near the midplane.

planetesimals, and planets. The planets grow by accreting much of the disk's solids and a little of its gas, so the ambient dust-to-gas ratio falls with time. Planets growing from Saturn- to Jupiter-mass pass from conditions resembling our 10S0 model to those more similar to the 5J2 model. The magnetic coupling regime in the deepening gap becomes less favorable to Hall

shear and more favorable to a magnetocentrifugal wind, so the field realigns. Much of the toroidal component is expelled, while the vertical flux is retained due to the constraints of the surrounding disk and wind. As a result, the mass flow onto the planet slows.

We have considered disks with a single planet. A second planet, interior to the first, could open a gap of its own, with the rim casting an X-ray shadow if the disk is not too flared. An inclined interior planet also could warp the disk nearer the star, creating a lighthouse effect where more X-rays reach the planet alternately from one side of the disk and then the other.

Although we have neglected the gradient term in the mass flow–stress relation (Equation (5)) when estimating the field strengths needed to drive the flows, this term could dominate around planet-opened gaps, where the diffusivities and hence the magnetic fields may change over distances comparable to the density scale height. In the simple model disk we used, the mass flow rate changes across the planet's orbit. If conditions vary sharply near the planet, the diffusivity will likewise have steep gradients. Magnetic fields have been shown to evolve toward a more nearly uniform radial profile than the gas in ideal-MHD, unstratified MRT calculations (Zhu et al. 2013). Evaluating the magnetic gradients in a more diffusive environment with radial and vertical structure in the ionization state will require further detailed MHD calculations. While 3D MHD models of disks with planet-opened gaps have been constructed including the ohmic diffusivity (Gressel et al. 2013), it now seems that the ambipolar and Hall terms are more important still.

We are grateful to Barbara Ercolano for advice on the X-ray opacities, Wilhelm Kley and Stephen Lubow for advice on the depths of planet-opened gaps, and Satoshi Okuzumi for providing his subroutine implementing the Bethell & Bergin cross sections. Lynne Hillenbrand's sponsorship of S.Y.K. at Caltech enabled this work to begin. The research was carried out in part at the Jet Propulsion Laboratory, California Institute of Technology, under a contract with the National Aeronautics and Space Administration, and with the support of the NASA Origins of Solar Systems program through grant 13-OSS13-0114 and Exoplanets Research Program through grant 17-XRP17_2-0081. Government sponsorship acknowledged.

ORCID iDs

S. Y. Kim https://orcid.org/0000-0001-7052-6647
N. J. Turner https://orcid.org/0000-0001-8292-1943

References

Bai, X.-N. 2011, ApJ, 739, 50
Bai, X.-N. 2014, ApJ, 791, 72
Bai, X.-N., & Goodman, J. 2009, ApJ, 701, 737
Baruteau, C., Crida, A., Paardekooper, S.-J., et al. 2014, in Protostars and Planets VI, ed. H. Beuther et al. (Tucson, AZ: Univ. Arizona Press), 667
Bethell, T. J., & Bergin, E. A. 2011a, ApJ, 740, 7
Bethell, T. J., & Bergin, E. A. 2011b, ApJ, 739, 78
Bjorkman, J. E., & Wood, K. 2001, ApJ, 554, 615
Cleeves, L. I., Adams, F. C., & Bergin, E. A. 2013, ApJ, 772, 5
Cleeves, L. I., Bergin, E. A., Qi, C., Adams, F. C., & Öberg, K. I. 2015, ApJ, 799, 204
D'Antona, F., & Mazzitelli, I. 1994, ApJS, 90, 467
Dürmann, C., & Kley, W. 2015, A&A, 574, A52
Ercolano, B., & Glassgold, A. E. 2013, MNRAS, 436, 3446
Feigelson, E. D., & Montmerle, T. 1999, ARA&A, 37, 363
Fung, J., & Chiang, E. 2016, ApJ, 832, 105
Fung, J., Shi, J.-M., & Chiang, E. 2014, ApJ, 782, 88
Garmire, G., Feigelson, E. D., Broos, P., et al. 2000, AJ, 120, 1426
Glassgold, A. E., Najita, J., & Igea, J. 1997, ApJ, 480, 344
Gressel, O., Nelson, R. P., Turner, N. J., & Ziegler, U. 2013, ApJ, 779, 59
Hawley, J. F., Gammie, C. F., & Balbus, S. A. 1995, ApJ, 440, 742
Hayashi, C. 1981, PThPS, 70, 35
Igea, J., & Glassgold, A. E. 1999, ApJ, 518, 848
Ilgner, M., & Nelson, R. P. 2006, A&A, 445, 205
Karzas, W. J., & Latter, R. 1961, ApJS, 6, 167
Keith, S. L., & Wardle, M. 2015, MNRAS, 451, 1104
Lesur, G., Kunz, M. W., & Fromang, S. 2014, A&A, 566, A56
Lin, D. N. C., & Papaloizou, J. 1986, ApJ, 309, 846
Lubow, S. H., & D'Angelo, G. 2006, ApJ, 641, 526
Lucy, L. B. 1999, A&A, 344, 282
Okuzumi, S., & Hirose, S. 2011, ApJ, 742, 65
Perez-Becker, D., & Chiang, E. 2011, ApJ, 735, 8
Preibisch, T., Ossenkopf, V., Yorke, H. W., & Henning, T. 1993, A&A, 279, 577
Safier, P. N. 1993, ApJ, 408, 115
Sano, T., & Inutsuka, S.-i. 2001, ApJL, 561, L179
Sano, T., Inutsuka, S.-i., Turner, N. J., & Stone, J. M. 2004, ApJ, 605, 321
Sano, T., & Stone, J. M. 2002, ApJ, 570, 314
Siess, L., Dufour, E., & Forestini, M. 2000, A&A, 358, 593
Turner, N. J., Choukroun, M., Castillo-Rogez, J., & Bryden, G. 2012, ApJ, 748, 92
Turner, N. J., & Sano, T. 2008, ApJL, 679, L131
Turner, N. J., Sano, T., & Dziourkevitch, N. 2007, ApJ, 659, 729
Umebayashi, T., & Nakano, T. 2009, ApJ, 690, 69
Wardle, M. 2007, Ap&SS, 311, 35
Weidenschilling, S. J. 1977, Ap&SS, 51, 153
Zhu, Z., Stone, J. M., & Rafikov, R. R. 2013, ApJ, 768, 143